

N O T I C E

THIS DOCUMENT HAS BEEN REPRODUCED FROM
MICROFICHE. ALTHOUGH IT IS RECOGNIZED THAT
CERTAIN PORTIONS ARE ILLEGIBLE, IT IS BEING RELEASED
IN THE INTEREST OF MAKING AVAILABLE AS MUCH
INFORMATION AS POSSIBLE

(NASA-TM-81283) PERFORMANCE AND ANALYSIS OF
A THREE-DIMENSIONAL NONORTHOGONAL LASER
DOPPLER ANEMOMETER (NASA) 42 p
HC A03/MF A01

N81-28390

CSSL 20D

Unclas
G3/34 26972

Performance and Analysis of a Three-Dimensional Nonorthogonal Laser Doppler Anemometer

Philip K. Snyder, Kenneth L. Orloff,
and Kiyoshi Aoyagi

July 1981



National Aeronautics and
Space Administration

Ames Research Center
Moffett Field, California 94035

Performance and Analysis of a Three-Dimensional Nonorthogonal Laser Doppler Anemometer

Philip K. Snyder

Kenneth L. Orloff

Kiyoshi Aoyagi, Ames Research Center, Moffett Field, California



National Aeronautics and
Space Administration

SYMBOLS

B	= Spacing of beam pair at reference station
D	= jet diameter
$g(y)$	= polynomial curve fit giving $\sin \frac{\beta}{2}$
H	= spacing between violet and green beam pairs at reference station
$h(y)$	= polynomial curve fit giving coupling angle ϕ
N	= number of samples
R	= distance from reference station to crosspoint of laser beams
R_D	= Reynolds number based on crossflow and jet diameter
$s_{BL,GN,VT}$	= sample standard deviation of measured velocity distributions for V_{BL} , V_{GN} , or V_{VT}
s_U	= estimator of population standard deviation for distribution of U; sample standard deviation
U,V,W	= general velocity components in x, y, z coordinate directions
$\bar{U}, \bar{V}, \bar{W}$	= mean velocity components in x, y, z coordinate directions
U_i, V_i, W_i	= particular instantaneous velocity components in x, y, z coordinate directions
U_∞	= free-stream velocity; crossflow
V_{BL}, V_{GN}, V_{VT}	= measured velocities from blue, green, and violet beam pairs
\bar{V}_R	= mean resultant velocity vector in y-z plane
$\Delta \bar{V}$	= uncertainty in mean value V
X,Y,Z	= Cartesian coordinates
z_c	= confidence coefficient; 1.96 for 95% confidence level
$\beta_{BL,GN,VT}$	= beam pair intersection angles
η	= $\frac{s_V}{s_{BL}}$ or $\frac{s_V}{s_{GN}}$
θ	= angle of resultant vector V_R from the vertical
$\Delta \theta$	= directional uncertainty of vector V_R in the y-z plane

- $\lambda_{BL,GN,VT}$ = wavelength of laser light
- σ = turbulence parameter \sqrt{U}
- τ = inclination angle of LDA system
- ϕ = coupling angle; angle between axes of green and violet beam pairs

PERFORMANCE AND ANALYSIS OF A THREE-DIMENSIONAL NONORTHOGONAL LASER DOPPLER ANEMOMETER

Philip K. Snyder, Kenneth L. Orloff, and Kiyoshi Aoyagi

Ames Research Center

SUMMARY

A three-dimensional laser Doppler anemometer (3D LDA) with a nonorthogonal third axis coupled by 14° has been designed and tested. An analysis of the statistical and systematic errors established the limitations of the 3D LDA. A highly three-dimensional flow field, a jet in a crossflow, was surveyed to test the three-dimensional capability of the instrument. Sample data are presented demonstrating the ability of the 3D LDA to resolve three orthogonal velocity components to within the theoretically predicted accuracy in several regions of the flow field. Modifications to the optics, signal processing electronics, and data reduction methods are suggested for further improving the accuracy of the 3D LDA.

INTRODUCTION

During the past decade, the laser Doppler anemometer (LDA) has become a useful instrument for the study of fluid-dynamic flows. By 1970, the simplification of dual-scatter optics had become commonplace (refs. 1-3) and many single-channel instruments were in operation. In 1973, a technique was reported (ref. 4) for using the two strongest output lines (514.5 and 488.0 nm) of an argon-ion laser to form two dual-scatter patterns that result in two independent orthogonal velocity measurements. Since that time, the two-color approach has been refined to the point where accurate, reliable commercial units are now available.

Unfortunately, the evolution of acceptable LDA optical systems for simultaneously measuring all three velocity components has not been quite as rapid. The earliest 3D instrument was reported in 1968 by Fridman et al. (ref. 5). This was a local-oscillator-type instrument in which three nearly on-axis detectors were used; the result was a matrix of three equations from which each of the orthogonal velocity components could be extracted. As a result, the instrument had exceptional sensitivity to velocity along the optical axis but lacked accuracy in measuring velocity in the transverse plane normal to the optical axis.

In contrast, the dual-scatter arrangement can accurately measure velocity components in the plane normal to the optical axis, but is insensitive to the on-axis velocity component. The most desirable 3D configuration would be a third (dual-scatter) channel whose optical axis would be aligned at right

angles to the 2D optical axis. Because such a system would have the distinct advantage of measuring all three velocity components orthogonally instead of resolving a third velocity component from two velocities coupled by an angle of less than 90° , it would be far from optimum from an applications point of view, especially for large flow facilities.

A combined LDA using the dual-scatter technique for the two orthogonal transverse velocity components with a single local-oscillator channel for the on-axis component would appear to provide the optimum with respect to component isolation and velocity sensitivity. Such a combined approach was reported in 1973 by Orloff and Logan (ref. 6). The major drawbacks to this approach were (1) the precision with which the local-oscillator beam must be aligned to insure proper heterodyning (ref. 7), and (2) the large excursions in Doppler shift frequency for only small variations in the on-axis velocity component. Moreover, the on-axis configuration has poor spatial resolution, especially when direct back- or forward-scatter detection is employed. On the other hand, the dual-scatter method incorporates both simplified alignment and high spatial resolution.

Accordingly, fully three-dimensional instruments that have recently been developed tend to utilize the dual-scatter arrangement nearly exclusively. Also, to eliminate crosstalk between the LDA channels and to more fully utilize the available output power of argon-ion lasers, the 476.5-nm line has been chosen for the third channel in favor of using polarization isolation. Abbiss et al. (ref. 8) have reported the application of such an instrument to trailing vortex flows, using photon correlation signal processing. An accurate system with the third component sensing orthogonally to the other two components by projecting in from the top of the wind tunnel, has been developed (private communication from J. F. Meyers, Langley Research Center, NASA). Yanta (ref. 9) has reported on a three-color system for the measurement of the 3D vortex patterns above a missile body at high angles of attack.

The development of a similar three-dimensional, three-color laser Doppler anemometer is reported here. Whereas the above mentioned 3D systems are fixed-focus (test-point position remains fixed relative to the output and receiving optics), a salient feature of the present instrument is the optical-mechanical scanning capability that has been incorporated to implement automated test-point positioning. The application of this instrument to a highly three-dimensional aerodynamic flow problem is presented as an example of system performance and limitations.

DESIGN PHILOSOPHY OF 3D LDA

The 3D LDA system described here was designed to be a versatile instrument applicable to many aerodynamic tests performed in the 7- by 10-Foot Subsonic Wind Tunnel at Ames Research Center. The system incorporates three distinguishable dual-scatter channels that provide for the measurement of three components of velocity. The distinguishability is accomplished through the use of three discrete output colors from an argon-ion laser. This makes

possible the detection of three corresponding velocity signals through the use of color-separating mirrors and filters in the receiving portion of the system. This technique results in efficient isolation of three signals with no detectable crosstalk. The optical portion of the instrument was designed to be mounted on an automated positioning platform located in front of the tunnel window. All six laser beams are transmitted through a single window that is part of the test-section wall. These six output beams occupy a small enough region of the optical window so that the LDA system can still be translated over a distance of 1 m in the vertical and streamwise directions. To realize the third axis of test-point positioning, a combined optical-mechanical technique is used to scan all six beams across the test section. Because particle-scattered light is collected in a backscatter mode through the same optics, the LDA system can be used with many different wind-tunnel models and model installations.

Three-dimensionality is achieved by the addition of a third single-channel backscatter LDA to a conventional 2D backscatter LDA. The added channel has only the argon laser source in common with the other channels. It is incorporated into the 2D system by suspending the new optical lens system above the other by means of a support structure and a tilting platform along with the appropriate mechanical apparatus for moving the new beams. The new single component can be instructed by computer to focus and tilt so that the measuring volumes of the 2D system and the additional 1D system coincide.

At the measuring volume, the 1D system measures a velocity vector that is coupled through a small angle (nominally 14°) to a vertical velocity vector measured with the 2D portion of the LDA. The velocity measured with the 1D system contains some information about a third velocity component that is orthogonal to the components measured by the 2D system. This third component may be resolved, in general, with greater accuracy for larger coupling angles; however, Orloff and Olson (ref. 10) and Corsiglia et al. (ref. 11) have reported acceptable results with coupling angles of 25° and 30° , respectively.

DESCRIPTION OF SYSTEM

Optical System

Figure 1 shows the optical layout of the 3D LDA. Major components of the 3D LDA are: (1) a 4-W argon-ion laser, (2) a series of dense flint prisms for color separation, (3) Bragg cells for frequency shifting, (4) a three-module scanning-lens system achromatized for two-color operation, (5) a support structure elevating a second three-element scanning-lens system optimized for operation at a third color, (6) a dichroic mirror and interference filters for color separation of collected light, (7) focusing lenses and pinholes for rejection of unwanted light, and (8) phototubes for light detection.

The argon-ion laser is equipped with blue-enhanced mirrors allowing the normally weaker 476.5 and 488.0 nm lines to lase with more power relative to the green 514.5-nm line. Hereinafter, the 476.5 nm line will be referred to as violet, the 488.0-nm line as blue, and the 514.5-nm line as green.

Using three equilateral prisms to sequentially disperse the laser light, adequate spatial separation of the violet, blue, and green beams is achieved in a short distance. Further separation is accomplished by a larger prism. Blue and green beams emerge parallel and about 10 cm apart and the violet beam is deflected (by a special prism) toward a tower that contains components for the third dimension of the instrument.

Both blue and green beams are directed to a beam-splitter/acousto-optic module. One of the split beams is shifted by 40 MHz and the two beams emerge from the unit with a vertical orientation for sensing vertical velocities; the blue beam pair emerge with a horizontal orientation for sensing stream-wise velocities.

Both blue and green beam pairs are directed by a set of mirrors to a three-module scanning-lens system intercepting the first lens in a square pattern; all beams are parallel to each other. By moving the rearmost lens module over a small distance (± 4 cm), the test point can be positioned from 0.9 to 3.8 m. The best focus distance is at 1.3 m from the output-lens face.

The violet beam is isolated through the dispersion prism and directed toward a lens-support structure designed to perform the 3D function of the LDA. The support structure elevates a tilting platform on which a second lens system is mounted. A small mirror directs the violet beam upward through a beam-splitter/Bragg-cell module mounted inside the structure. A strip mirror intercepts the two emerging violet beams and aligns them with the scanning lens system. Because the lens system must tilt — in order to position the measuring volume so that it is coincident with that of the 2D lens system — the strip mirror is designed to rotate with the lens system at half the rate of the tilting platform. This is done with a mechanical reducer that must be precisely adjusted to maintain alignment of the beams relative to the axis of the lens system. The lens system will focus the beams through a range of 0.9 to 3.6 m from the lens face with the best focus distance occurring at 1.1 m. The complete range of the LDA system is 1.1 to 3.3 m, measured from the 2D lens face, with coupling angles from 16.0° to 5.5° , respectively. Scanning of both lens systems and tilting of the 3D platform is accomplished with high-resolution stepping motors and zero backlash lead screw. Position readback is through optical encoders.

Collection of particle-scattered light is done in a backscatter mode through the same optics used for transmitting the laser beams into the flow field. Blue and green scattered light, collected through the common lens system, must be separated before focusing at the photodetectors. This is accomplished with a dichroic mirror that reflects blue light and transmits green light. Each color is then separately directed and focused onto a pin-hole (0.7 mm) for spatial filtering; channel isolation is assured by using narrow-band interference filters designed for the appropriate wavelength of

light at the respective phototubes. Independent phototubes detect the blue and green light. The violet light is received through the elevated lens system from where it was originally transmitted rather than using the lower lens system to collect it for detection along with the blue and green light. The latter method is not practical because the violet measuring volume would have to be exactly coincident with the blue and green measuring volumes at all times in order to process the violet light through the lower lens system. The violet light is therefore collected through the upper lens system and focused onto a third pinhole, interference filter, and phototube.

System Electronics

The electronics for the 3D LDA serves three main functions — processing LDA signals, automating all mechanical motion, and reducing data. Figure 2 is a block diagram showing the various kinds of electronics to be described.

Major components of the system electronics are (1) signal conditioning electronics (e.g., amplifiers, down-mixers, and filters); (2) countertype signal processors, including an oscilloscope and spectrum analyzer for signal monitoring; (3) a digital computer for data management and automation; (4) a motor control interface and motor power supplies; and (5) motors and encoders for moving the translation platform and positioning the "zoom" lenses and the tilting platform.

Single-particle burst signals from the phototubes are high-pass-filtered and amplified. They are then electronically down-mixed to obtain signal frequencies within a range that can be more accurately measured with the countertype processors.

The processors accept the down-mixed signal and provide additional high-pass and low-pass filtering (selectable) as well as amplification. Both digital and analog outputs are available from the counter processor. The analog output is used as a visual monitor (an oscilloscope) to indicate the presence of noise and the degree of turbulence. A spectrum analyzer is used to verify that the frequency generated by the counter is indeed the correct value as well as indicating the signal/noise ratio and presence of turbulence. The digital outputs from the three counters are connected through an interface to a dedicated minicomputer-based data acquisition and control system.

The computer and LDA interface along with additional analog and digital channels compose the data processing system. A graphics terminal provides user-interactive access to the main computer as well as display of data in graphical form. Control of the LDA translating platform as well as focusing of the lens systems is accomplished through an additional motor control interface. The interface allows the computer to control five stepping motors. Position readback is through optical encoders, thereby forming a closed-loop, motor-encoder control system. The interface cabinet also includes all necessary power supplies for the stepping motors.

3D LDA System Positioning

The 3D LDA is mounted on a translating platform (fig. 8) that locates the entire optical system in the vertical and horizontal directions. The 3D LDA is raised and lowered (z-motion) with four ball screws located at the four corners of the platform base and driven with a single belt from a stepping motor. Alignment is maintained with four vertical linear bearings. Horizontal motion (x-motion) is provided with a single ball screw driven by a second stepping motor. Two horizontal linear bearings support the entire structure. The travel limits for the platform are 100 cm in the vertical direction and 90 cm in the horizontal direction. Positioning accuracy is within 0.1 mm, repeatable for both vertical and horizontal axes.

DATA REDUCTION

Recording Data

Particles in the flow field pass through the intersections of the laser beams of the 3D LDA. The resulting bursts of light being detected contain useful frequency information which is measured by a counter processor and interpreted by a computer to give the speed of the particles. Each burst from a particle represents one data point that is recorded in memory by a computer. Many samples must be recorded to obtain a distribution from which a sample mean and standard deviation may be computed.

Data samples from the blue, green, and violet channels were accepted on a first-come, first-serve basis. A data point consisted of collecting 100 samples (sometimes 200) of data for each channel. The collection time for a data point was limited by the data collection rate of each channel. Mean velocities were computed by averaging a set of N samples as follows:

$$\bar{U} = \frac{1}{N} \sum_{i=1}^N U_i \quad (1)$$

A best estimate for the standard deviation of the sample was computed as

$$s_U = \left[\frac{\sum_{i=1}^N (U_i - \bar{U})^2}{N - 1} \right]^{1/2} \quad (2)$$

Sample means and standard deviations were recorded in a file in the computer and categorized by beam color as \bar{V}_{GN} , \bar{V}_{BL} , and \bar{V}_{VT} and as s_{GN} , s_{BL} , and s_{VT} , respectively. These measured statistical parameters are the basic raw data from which mean velocities in other coordinate systems may be

computed. In addition, the standard deviations serve as quantitative indicators of the usefulness of the mean value to the experimenter.

It is necessary to clarify the statistical quantity s . Although it is often used to represent the turbulence in the flow field, it also reflects any broadening or skewing of the velocity sample distribution due to measurement problems. Even if measurements were perfect, Yanta and Smith (ref. 12) show that one would still require nearly 600 samples before the quantity s would represent the actual turbulence with 5% accuracy. In the following sections, s is used in several equations to help define confidence limits for the mean value \bar{U} . These limits are dependent on the actual turbulence present in the flow field as well as any additional apparent turbulence or biasing incurred in the measurement process.

Computation of Mean Velocities

Mean velocities in terms of an orthogonal reference coordinate system were determined from Doppler frequency information from three counter processors (blue, green, and violet) and from beam geometry specified as a function of the y coordinate. Velocities V_{BL} , V_{GN} , and V_{VT} are computed through the following equations:

$$V_{BL} = \frac{\lambda_{BL} f_{BL}}{2 \sin \beta_{BL}/2} = \frac{0.4880 f_{BL} \text{ (MHz)}}{2g_{BL}(y)} \quad (3)$$

$$V_{GN} = \frac{\lambda_{GN} f_{GN}}{2 \sin \beta_{GN}/2} = \frac{0.5145 f_{GN} \text{ (MHz)}}{2g_{GN}(y)} \quad (4)$$

$$V_{VT} = \frac{\lambda_{VT} f_{VT}}{2 \sin \beta_{VT}/2} = \frac{0.4765 f_{VT} \text{ (MHz)}}{2g_{VT}(y)} \quad (5)$$

where $g(y)$ is a polynomial curve fit for the sine of the beam pair intersection half-angle $\sin \beta/2$, f (MHz) is the Doppler frequency output from the counter processor, and λ is the wavelength of the corresponding beam color.

Figure 3 depicts the geometrical relationship between the measured velocities \bar{V}_{BL} , \bar{V}_{GN} , and \bar{V}_{VT} and the coordinates \bar{U} , \bar{V} , and \bar{W} . The transformation is given by

$$\bar{U} = \bar{V}_{BL} \quad (6)$$

$$\bar{V} = \bar{V}_{GN} \left[\sin \tau - \frac{\cos \tau}{\tan \phi} \right] + \bar{V}_{VT} \frac{\cos \tau}{\sin \phi} \quad (7)$$

$$\bar{W} = \bar{V}_{GN} \left[\cos \tau + \frac{\sin \tau}{\tan \phi} \right] - \bar{V}_{VT} \frac{\sin \tau}{\sin \phi} \quad (8)$$

where $\tau = 2.74^\circ$ is the fixed inclination angle of the LDA system relative to the reference coordinate system, and $\phi = h(y)$ is the coupling angle determined from a third-order polynomial curve fit.

Uncertainty Analysis

Statistical velocity component uncertainty- It is important to understand how the geometry of the nonorthogonal measurement axes illustrated in figure 3 fundamentally affect the accuracy of the computed orthogonal velocities \bar{U} , \bar{V} , and \bar{W} . In the following uncertainty analysis, the transformations giving \bar{U} , \bar{V} , and \bar{W} in terms of \bar{V}_{BL} , \bar{V}_{GN} , and \bar{V}_{VT} (eqs. (6)-(8)) will be further simplified by assuming that the inclination angle of the LDA system, τ , equals zero resulting in the following transformation equations:

$$\bar{U} = \bar{V}_{BL} \quad (9)$$

$$\bar{V} = \frac{\bar{V}_{VT}}{\sin \phi} - \frac{\bar{V}_{GN}}{\tan \phi} \quad (10)$$

$$\bar{W} = \bar{V}_{GN} \quad (11)$$

Estimation theory (refs. 13, 14) suggests that the mean value and its uncertainty may be written as $\bar{U} \pm z_c s_U / N^{1/2}$ where z_c is the confidence coefficient for a normal distribution. The uncertainty in the value of the mean $z_c s_U / N^{1/2}$ will be referred to as $\Delta \bar{U}$. For example, $z_c = 1.96$ gives a 95% confidence level that the measurement of the mean velocity is not in error by more than $\pm 1.96 s_U / N^{1/2}$. The uncertainties in the mean values \bar{U} and \bar{W} are simply, from equations (9) and (11), $\Delta \bar{V}_{BL}$ and $\Delta \bar{V}_{GN}$ or, equivalently, $z_c s_{BL} / N^{1/2}$ and $z_c s_{GN} / N^{1/2}$.

The lateral velocity \bar{V} is resolved from measurements of mean velocities \bar{V}_{GN} and \bar{V}_{VT} , as indicated by the transformation equation (10). Similarly, the uncertainty $\Delta \bar{V}$ of the lateral mean velocity will be expressed as $z_c s_V / N^{1/2}$ where s_V is a function of s_{GN} , s_{VT} , and the coupling angle ϕ . Assuming that the flow in the plane of \bar{V}_{VT} and \bar{V}_{GN} is such that the turbulence values s_{VT} and s_{GN} are approximately equal for small angles of ϕ (30° or less), then one can say that the estimators for the turbulence, s_{VT} and s_{GN} , are about equal. With this assumption, as well as the knowledge that instantaneous measurements of V_{VT1} and V_{GN1} are independent of each other (i.e., were sampled at different times rather than simultaneously), an expression for s_V is

$$s_V = s \frac{(1 + \cos^2 \phi)^{1/2}}{\sin \phi} \quad (12)$$

where s is either s_{VT} or s_{GN} . It is convenient to define a ratio η to be s_V/s so that,

$$\eta = \frac{(1 + \cos^2 \phi)^{1/2}}{\sin \phi} \quad (13)$$

A complete derivation of this expression is presented in appendix A. Basically, this says that a distribution of velocities $V_i (i = 1, \dots, N)$ can be obtained from

$$V_i = \frac{V_{VTi}}{\sin \phi} - \frac{V_{GNI}}{\tan \phi} \quad (14)$$

by randomly grouping pairs of independent measurements of V_{VT} and V_{GN} . The resulting distribution will be broader than either of the distributions V_{VTi} and V_{GNI} . Specifically, the distribution for V will be broader by the factor η .

The uncertainty $\Delta \bar{V}$ may now be written as

$$\Delta \bar{V} = \frac{z_c s_V}{N^{1/2}} = \frac{z_c \eta s}{N^{1/2}} \quad (15)$$

From equation (13), a nominal coupling angle ϕ of 14° gives $\eta = 5.75$. Hence the uncertainty $\Delta \bar{V}$ in the lateral mean velocity \bar{V} is expected to be almost 6 times greater than the uncertainty $\Delta \bar{W}$ in the vertical mean velocity.

Based on 100 data samples and a confidence level of 95% ($z_c = 1.96$), the estimated uncertainties in the three orthogonal velocity components \bar{U} , \bar{V} , and \bar{W} in terms of estimated standard deviations s_{BL} , s_{GN} , and s_{VT} will be

$$\Delta \bar{U} = 0.196 s_{BL} \quad (16)$$

$$\Delta \bar{V} = 1.13 s_{GN} \text{ or } s_{VT} \quad (17)$$

$$\Delta \bar{W} = 0.196 s_{GN} \quad (18)$$

Statistical velocity direction uncertainty- An alternative way of looking at the precision of the 3D LDA, which is significant for the purpose of mapping a flow field, is to consider the directional uncertainty of a resultant vector \bar{V}_R in each of three possible planes x-y, y-z, and x-z. For the 3D LDA, special consideration is given to the resultant vector in the y-z plane since it is in this plane that the velocity component coupling occurs.

A resultant vector \bar{V}_R residing in the y-z plane has a direction θ from the z-axis and a directional uncertainty $\Delta \theta$. It can be shown (appendix B) that for a given number of samples N and relative standard deviation s/\bar{V}_R , the directional uncertainty $\Delta \theta$ is given by

$$\Delta \theta (\text{rad}) = \frac{z_c}{N^{1/2}} \frac{s}{\bar{V}_R} \cos \theta \left(\eta^2 + \tan^2 \theta + \frac{2 \tan \theta}{\tan \phi} \right)^{1/2} \quad (19)$$

Using this expression, the curves of figures 4 and 5 have been generated.

For a 95% confidence level, and a typical relative standard deviation s/\bar{V}_R equal to 30% ($s = s_{GN} = s_{VT}$), figure 4 suggests that 1500 velocity samples are required to resolve a vertical vector, $\theta = 0^\circ$, to within $\pm 5\%$. However, only 50 samples are required to resolve a horizontal vector, $\theta = 90^\circ$, to the same accuracy. On the other hand, if a directional uncertainty of $\pm 10^\circ$ is acceptable, the number of samples required for resolving a vertical vector is only 400, and for a horizontal vector as low as 11. For $N = 100$ (typical for data presented later), figure 5 shows the directional uncertainty $\Delta\theta$ as a function of θ for several relative standard deviations. Notice that directional uncertainties can be as high as $\pm 20^\circ$ for vertical vectors with $s/\bar{V}_R = 0.30$ and as low as $\pm 3^\circ$ for a horizontal vector.

Figure 5 also demonstrates that the standard deviation significantly affects the directional uncertainty $\Delta\theta$. The standard deviation is representative of not only the turbulence present within the flow field but also reflects noise present during signal processing. Because the accuracy of the 3D LDA is so strongly influenced by large standard deviations, attempts should be made to fully optimize the system and minimize the possibility of processing errors due to noise.

Systematic velocity uncertainties- Many methods have been proposed for LDA calibration. One such method is shown in figure 6. The drawing depicts the arrangement of the green and violet beams of the 3D LDA designed to sense two nonorthogonal components of velocity, \bar{V}_{GN} and \bar{V}_{VT} . From these velocities, the orthogonal velocity components \bar{V} and \bar{W} may be computed from equations (10) and (11) (repeated here):

$$\bar{V} = \frac{\bar{V}_{VT}}{\sin \phi} - \frac{\bar{V}_{GN}}{\tan \phi} \quad (10)$$

$$\bar{W} = \bar{V}_{GN} \quad (11)$$

The velocities \bar{V}_{VT} and \bar{V}_{GN} are computed from the averages of N samples of the instantaneous velocities \bar{V}_{VT} and \bar{V}_{GN} from the familiar LDA equations (also repeated here):

$$V_{GN} = \frac{\lambda_{GN} f_{GN}}{2 \sin \beta_{GN}/2} \quad (4)$$

$$V_{VT} = \frac{\lambda_{VT} f_{VT}}{2 \sin \beta_{VT}/2} \quad (5)$$

The wavelengths, λ_{GN} and λ_{VT} , are known exactly; f_{GN} and f_{VT} are measured by processing electronics and β_{GN} and β_{VT} are computed from calibration measurements.

Calibration is accomplished by measuring the following values and absolute uncertainties:

$$R \pm \Delta R$$

$$B_{GN} \pm \Delta B_{GN}$$

$$B_{VT} \pm \Delta B_{VT}$$

$$H \pm \Delta H$$

All other distances and angles indicated in figure 6 are computed from the measured values.

Using equations (4) and (5) and geometric relationships from figure 6, it can be shown that

$$\frac{\Delta \bar{V}_{GN}}{\bar{V}_{GN}} = \frac{\Delta \bar{f}_{GN}}{\bar{f}_{GN}} + \frac{\Delta B_{GN}}{B_{GN}} + \frac{(1/4)B_{GN} \Delta B_{GN} + R \Delta R}{(1/4)B_{GN}^2 + R^2} \quad (20)$$

$$\frac{\Delta \bar{V}_{VT}}{\bar{V}_{VT}} = \frac{\Delta \bar{f}_{VT}}{\bar{f}_{VT}} + \frac{\Delta B_{VT}}{B_{VT}} + \frac{(1/4)B_{VT} \Delta B_{VT} + H \Delta H + R \Delta R}{(1/4)B_{VT}^2 + H^2 + R^2} \quad (21)$$

It can also be shown from equation (10), by rewriting it in polar form, that

$$\frac{\Delta \bar{V}}{\bar{V}_R} = A(\phi) \cos \theta + B(\phi) \sin \theta \quad (22)$$

where

$$A(\phi) = \frac{1}{\tan \phi} \left[\frac{\Delta \bar{V}_{VT}}{\bar{V}_{VT}} + \frac{\Delta \bar{V}_{GN}}{\bar{V}_{GN}} + \frac{\Delta H}{H} (2 + \sin^2 \phi) + \frac{\Delta R}{R} (1 + \cos^2 \phi) \right]$$

$$B(\phi) = \frac{\Delta \bar{V}_{VT}}{\bar{V}_{VT}} + \frac{\Delta H}{H} (1 + \sin^2 \phi) + \frac{\Delta R}{R} \cos^2 \phi$$

where \bar{V}_R is the resultant velocity in the y-z plane and θ is the vector direction measured from the vertical. In equation (22), $\Delta \bar{V}/\bar{V}_R$ is the uncertainty in the lateral velocity component relative to the in-plane velocity vector; for a given LDA arrangement (fixed ϕ), $\Delta \bar{V}/\bar{V}_R$ depends strongly on θ .

Using equations (20), (21), and (22), the systematic uncertainties for all three LDA channels can be determined. The terms $\Delta \bar{f}/\bar{f}$ in equations (20)

and (21) can be considered small compared with the remaining terms because of the high accuracy of the counter processors and the large number of samples acquired for each mean.

The following values and absolute uncertainties were typical for the 3D LDA:

$$R = 90 \pm 0.2 \text{ cm}$$

$$B_{VT} = 11.7 \pm 0.1 \text{ cm}$$

$$B_{GN} = 12.0 \pm 0.1 \text{ cm}$$

$$H = 22.5 \pm 0.2 \text{ cm}$$

Substituting these values into equations (20), (21), and (22) yields

$$\Delta \bar{V}_{GN} / \bar{V}_{GN} = 0.011$$

$$\Delta \bar{V}_{VT} / \bar{V}_{VT} = 0.011$$

$$\Delta \bar{V} / \bar{V}_R = 0.179 \cos \theta + 0.014 \sin \theta$$

The blue LDA channel is treated in the same way as the green channel; therefore, $\Delta \bar{V}_{BL} / \bar{V}_{BL} = 0.011$.

From equations (9), (10), and (11), the systematic uncertainties for measurements of the orthogonal velocities \bar{U} , \bar{V} , and \bar{W} are

<u>Component</u>	<u>Relative uncertainty</u>
\bar{U}	$\Delta \bar{U} / \bar{U} = 1.1\%$
\bar{W}	$\Delta \bar{W} / \bar{W} = 1.1\%$
$\bar{V}(\theta = 0^\circ)$	$\Delta \bar{V} / \bar{V}_R = 18\%$
$\bar{V}(\theta = 45^\circ)$	$\Delta \bar{V} / \bar{V}_R = 14\%$
$\bar{V}(\theta = 90^\circ)$	$\Delta \bar{V} / \bar{V}_R = 1.4\%$

APPLICATION OF THE 3D LDA TO A JET IN A CROSSFLOW

Test Description

The 3D LDA was installed in the 7- by 10-Foot Wind Tunnel at Ames Research Center for measurement of the flow field associated with a high-speed jet in a crossflow. Figure 7 is a conceptual drawing of the jet in a

crossflow. The diversity of this flow, for example, higher shear regions, wake regions, potential flow, and vortices, provided an environment in which the performance and practicality of the 3D LDA could be evaluated.

The jet in a crossflow model consists of a 50-mm (2-in.) diameter outlet in the surface of a suspended ground plane (fig. 8). A plenum and converging nozzle are aligned below the ground plane to generate an air jet of uniform profile that emerges 90° to the ground plane. The jet is situated 90 cm from an optical window that forms one side of the wind-tunnel test section. The height of the ground plane from the test section floor is 90 cm. An airfoil-shaped fairing surrounds the plenum, resulting in a streamlined model.

The air jet is seeded by injecting an oil mist into the plenum chamber. Mineral oil is dripped on a heating element and shop air carries the resulting oil mist into the plenum chamber. The mist is introduced through four equally spaced nozzles positioned around the plenum in an attempt to distribute the particles as uniformly as possible in the jet. The wind-tunnel air (crossflow) is seeded by using a fluid atomizer and injecting particles into the tunnel downstream of the test section. Mineral oil is again used to produce the fluid particles.

The particle-size distribution from the fluid atomizer has been measured (engineering report by M. Doty et al., Ames Research Center, NASA); most of the particles were found to be less than 3 μm in diameter. The particles were small enough that there was little doubt of their following the airflow. The particle sizes generated by the heating element were unknown, but signal performance was similar when the illumination in the jet was about equal to the illumination in the free stream.

Beam Calibration

A reference coordinate system was oriented so that its origin was in the ground plane and centered in the jet. The streamwise direction was designated as positive x . The horizontal direction perpendicular to the stream and away from the LDA was designated as positive y . The vertical direction, upwards, was designated positive z . To apply the 3D LDA to the jet in a crossflow experiment and obtain data near the ground plane, it was necessary to incline the LDA scanning axis with respect to the lateral axis of the tunnel. This was done by setting the entire optical system angle, τ , at 2.74°, as indicated in figures 8 and 9. At this angle, the lower green beam did not contact the ground plane when the measuring volume was positioned over the jet and close to the plate.

Positioning of the measuring volume was accomplished by moving the LDA package vertically and streamwise with a translation system (fig. 8), and in the lateral direction by optically scanning the laser beams. Vertical and streamwise motions are uncoupled from the other motions; their calibration involves determining constants that define linear relationships of coordinate locations to computer counts. The only significant error in vertical and

streamwise positioning is a fixed offset due to the uncertainty in setting initial reference points. This error is estimated to be within 0.5 mm.

Lateral positioning is a four-motor operation. Separate motors are used to scan the 2D and 1D zoom-lens systems to change the respective focus distances. A third motor tilts the 1D lens system, aligning the focus so that it is coincident with that of the 2D lens system. The vertical motion motor compensates for a change in vertical position that results from scanning laterally along a tilted axis (angle τ). The scanning and tilting operations involve nonlinear relationships between lateral position and computer counts. Hence polynomial curve fits are needed to enable the computer to position the focused beam pairs on a single spot. Calibration involves manually setting the crossing point of the blue, green, and violet beam pairs at a known lateral location and recording the computer counts. After recording counts for 10 lateral locations within 15 cm of the jet, constants for a third-order polynomial are determined by a method of least squares. Errors inherent in the scanning mechanism and from the polynomial curve fits were insignificant compared with the uncertainties in visually locating the lateral coordinates.

Mechanical backlash introduced some error in positioning the violet beam pair emerging from the 1D tilting lens system. The backlash problem was minimized by an appropriate algorithm that would move the tilt motor so as to approach the desired location from one direction only. Using this technique, acceptable positioning of the violet beam pair was possible, and uncertainties in vertical spot placement within 0.5 mm were obtained.

The estimated limits of uncertainty in positioning the blue, green, and violet beam pairs on a single spot are represented by the region illustrated in figure 10. The measuring volumes for each beam pair can be expected to reside within the volume bounded by this box; the desired coordinate location is defined to be the midpoint of this volume. Overall positioning uncertainties are therefore 0.5 mm for vertical placement, 0.5 mm for streamwise placement, and 1 mm for lateral placement.

Sample Data

Most of the data in the jet in a crossflow test were taken near the base of the jet to study the entrainment effect near the plate. Acceptable results were obtained near the wake of the jet as well as in the upstream and accelerated flow regions around the jet. Attempts were made to collect data inside the jet and through the shear regions; however, limitations due to the small coupling angle combined with several optical and signal processing problems resulted in poor data. The limitations imposed by the optics and electronics are not fundamental in nature, and future modifications will result in a system that will perform better in complex flow regions.

Three velocity surveys are presented graphically in figures 11 through 13. These data were relatively free from problems involving alignment, seeding, or signal processing. The areas around the jet where surveys were made

are therefore representative of the kinds of flows that can be measured successfully with the 3D LDA as implemented. Vector plots in the y - z plane for each velocity survey are presented in figures 14 through 16. These plots show the statistical directional uncertainties for each vector as computed from equation (19).

The data shown graphically in figures 11 and 14 were collected as a lateral survey upstream of the jet. The predicted uncertainties for each data point, marked as confidence intervals, were computed from equations (16) through (18) using estimated standard deviations s_{BL} , s_{GN} , and s_{VT} . The approximate average relative uncertainties were $\Delta\bar{U}/\bar{U}_\infty = 0.02$, $\Delta\bar{V}/\bar{U}_\infty = 0.06$, and $\Delta\bar{W}/\bar{U}_\infty = 0.01$. The directional uncertainties $\Delta\theta$ in figure 14 range from 5° to 45° at the center of the survey, with relative standard deviations s_{GN}/\bar{V}_R from 11 to 69%.

Figures 12 and 15 show a lateral survey through a region of the flow field where high vertical velocities and high turbulence exist. The approximate relative uncertainties in the velocity components were $\Delta\bar{U}/\bar{U}_\infty = 0.06$, $\Delta\bar{V}/\bar{U}_\infty = 0.07$ to 1.17 , and $\Delta\bar{W}/\bar{U}_\infty = 0.12$ to 0.20 . From the large uncertainties in the lateral velocity component, it is evident that high turbulence is making it particularly difficult to achieve high accuracy with only 200 samples per data point. The directional uncertainties $\Delta\theta$ shown in figure 15 range from 2 to 19%. Relative standard deviations s_{GN}/\bar{V}_R are 12 to 41%, respectively.

Figures 13 and 16 are a lateral survey into the wake region of the jet. The approximate average relative uncertainties were $\Delta\bar{U}/\bar{U}_\infty = 0.04$, $\Delta\bar{W}/\bar{U}_\infty = 0.04$, and $\Delta\bar{V}/\bar{U}_\infty = 0.04$ to 0.40 . The high uncertainties in the lateral flow were due to the higher turbulence in the wake region. The directional uncertainties $\Delta\theta$ in figure 16 range from 2° to 29° . Relative standard deviations s_{GN}/\bar{V}_R are 7 to 47%, respectively.

Alignment Errors

The alignment of the laser beams, meaning specifically the precision with which the probe volumes for the various components overlap one another, is critical, especially in regions of high shear. One such region is the edge of the jet, where there is a transition from a vertical velocity ratio \bar{W}/\bar{U}_∞ of less than 1 to a velocity ratio of 8 or greater over a few millimeters. The basic problem involves the fact that the mean velocities computed from the green and violet beams must represent the same location in the flow field so that a meaningful lateral flow can be computed. If the green and violet beams are misaligned so as to measure velocities at slightly different locations in the flow field, and if the flow field involves velocity gradients that may be significant over the misalignment distance, then the computed lateral velocity may not be accurate.

Figure 17 shows a plot of the lateral flow for a y -survey which approaches the downstream edge of the jet. The data were manipulated to simulate a fixed misalignment of the green and violet beams to show how this

misalignment might affect the computed lateral velocity component. For the purpose of analyses, the original data are assumed to have been taken under conditions of perfect alignment, an assumption that may or may not be true.

The resulting shifts in lateral flow show a 20% variation in the data in areas of low mean shear, increasing to 50% in the high shear region near the edges of the jet. These high uncertainties limit the use of the instrument in shear flows unless the alignment of the beams can be controlled within acceptable limits. If such alignment cannot be obtained, it would not be advisable to scan optically in areas of high shear; instead, it would be better to translate the complete LDA package across the small shear region after a precision alignment of the green and violet beams.

SYSTEM IMPROVEMENTS

The performance of the 3D LDA could be greatly improved by optimizing the optical system; this would result in better light transmission efficiency and higher signal/noise ratios upon detection. Improvements to the electronics in terms of better filtering properties are essential to receiving high-quality signals with a good signal/noise ratio.

Optical

Weak signals from the violet channel (tilting beam pair) were found to be primarily a result of relatively low power in the output beams. Only 12 mW were measured in the violet beams as compared with 190 mW and 90 mW in the blue and green beams, respectively. The low power in the violet beams resulted in low data rates (around 30 samples per second) because the processor circuitry rejected many Doppler bursts with low signal/noise ratios. The blue and green channels produced relatively high data rates — 500 to 1000 samples per second. Because 100 samples were required in each channel, the low data rates in the violet channel resulted in a longer data acquisition time than was desirable.

There is normally lower power available to the 476.5-nm (violet) line from the argon laser; however, the main reason for low power is the losses in mirrors and prisms. Presently, the two mirrors being used for the violet beam are not optimized. Losses may be reduced by using dielectric high reflectance mirrors designed for a specific wavelength, polarization, and interception angle. The use of a polarization rotator designed for the correct wavelength will also minimize losses in the beam splitter prism.

The argon-ion laser was not optimized to deliver higher power in a Gaussian TEM 00 mode to all three colors. The laser power was set at nominally 2.5 W during the jet in a crossflow test; a higher operating power in the TEM 00 mode would create more output, particularly in the violet beam where it is needed. Experience with the 3D LDA described in this report suggests that a better mean value for the lateral component can be achieved by

using the two high-power beams, blue and green, to measure the lateral velocity component V . Presently, the green is used for the vertical velocity component and the violet beam for the tilted component. Interchanging the blue and violet beams so that the blue is used for the tilted beam would allow this optimum situation. Because the violet beam would then measure stream-wise flow, a higher uncertainty in this measurement would not propagate to the other components. This interchange involves only minor changes, and those changes are being implemented. The two scanning-lens systems will have to be redesigned to operate with the new wavelengths. The new lenses will also have to be designed to have an optimum focus at the center of the 7- by 10-Foot Wind Tunnel (since the present best focus is offset from the center by 60 cm).

Stray light on the surface of the phototubes was found to increase the noise level in the system. Most such light will be eliminated by redesigning a single mirror as well as using some black panels as shields.

Electronics

The major problem associated with the processing electronics involved a lack of flat response of the various filters and amplifiers. The frequency down-mixers were found to have a nonuniform frequency response across their spectrum. Also a rolloff at 22 MHz limited the use of the down-mixers to regions outside the jet; a rolloff of at least 35 MHz is desirable. (The frequency down-mixers are presently being modified to extend their frequency response range to 50 MHz with a flatness of ± 3 dB.) In addition, one of the counter processors was later found to have a malfunctioning input filter; this also caused uneven response. The end result of these problems was a loss of signal at certain frequencies. The data rate would drop as soon as the Doppler frequency coincided with a "low spot" in the spectrum. Also, in trying to process these signals, noise rejection was difficult; this resulted in biased mean values and artificially high standard deviations.

CONCLUSIONS

The suggested improvements to the optics and to the processing electronics will improve the quality of the LDA signals. The improved signal/noise level will result in better performance of counter processors and higher data rates. Improvements in the flatness of response in the down-mixers and counters will allow a maximum rejection of noise in the system resulting in more accurate standard deviations. The standard deviations should then better represent the nature of the flow rather than a combination of fluid and electronic properties; this will reduce some of the uncertainties in the data.

Estimation theory has shown that statistical errors are proportional to the standard deviation of the velocity sampling distribution and inversely proportional to the square root of the number of samples (ref. 14). Hence

the higher data rates and more accurate standard deviations that are expected from LDA system improvement should be effective in reducing the statistical uncertainties. With the improved data rates, a larger number of data samples can be collected in a given time; hence, it is not unreasonable to expect a 50% reduction in the estimated errors if the number of samples is increased from 100 to 500.

The systematic uncertainty analysis for the 3D LDA indicates a need for a more accurate calibration procedure. Although the vertical and streamwise velocity-component uncertainties are low ($\Delta W/W = \Delta U/U = 0.011$), the lateral-component uncertainties ($\Delta V/V_R = 0.18$) are high, especially where the flow direction in the y-z plane is primarily vertical. To increase the accuracy in the lateral velocity component, a calibration procedure must be devised that eliminates the need for accurate measurements of distances and angles of the laser beams. Ideally, a calibrated velocity source that can be used to determine calibration constants without knowledge of the angles between the beams is desirable. The construction of such a device for use with the 3D LDA is under consideration.

An obvious way to increase the accuracy of the lateral flow component would be to increase the coupling angle between the vertical velocity and the tilted component. As mentioned before, part of the philosophy of the 3D instrument involved the fact that all the transmitted and collected light passes through a single window and allows the instrument to translate vertically and horizontally with adequate motion. By increasing the coupling angle, one sacrifices vertical motion because the upper lens system must be raised. Since some tests do not require as much vertical motion, there is the possibility of making the height of the upper lens system variable to allow a range of coupling angles from 10° to 25° at the center of the tunnel. A coupling angle of 25° rather than 14° would result in a reduction of uncertainty in the lateral flow by 45%.

An understanding of the manner in which statistical uncertainties in the mean velocities and vector directions influenced the turbulence in the flow and the number of data samples acquired can be useful in optimizing the performance of the 3D LDA. By combining the statistical uncertainty equations presented in this report with the LDA data acquisition routines, one can specify the accuracy of the mean velocities to be a parameter for a flow survey; the software is thereby used to compute the required number of samples to meet this accuracy requirement. This method of operation would be optimum in the sense that no more samples would be taken than are necessary to a certain velocity component or vector direction accuracy. For example, in a laminar region of a flow, it may only be necessary to take 20 data samples rather than 100 data samples to achieve a 5% accuracy. However, in a turbulent region, 600 samples may be required to achieve the same accuracy. This kind of interactive programming along with the higher data rates available from improved optics and electronics could improve the efficiency of a velocity survey as well as provide a method for controlling and monitoring the accuracy of the 3D LDA.

Some recent calculations by Orloff and Snyder (submitted for publication) show that if the data for the vertical and tilted components of velocity are accepted as simultaneous pairs, and if computations of the lateral component are made independently for each data pair before averaging, then the resulting statistical uncertainty in the lateral mean component will be identical with that of the measured components. Orloff and Olson have been successful in taking data in simultaneous pairs through the use of an electronic simultaneity unit. This technique requires that the beams be precisely crossed, however, in order to simultaneously receive signals in more than one channel. For the 3D LDA described here, the precision of the optical mechanical scanning system is not adequate. On the other hand, to incorporate simultaneity, one could precisely align the 3D LDA optics at a fixed range and then translate the complete system. Data rates are significantly lower when processing simultaneous signals; however, calculations show that the gain in accuracy in the lateral velocity component is sufficient to justify accepting fewer data samples. This kind of signal processing will be investigated further and possibly incorporated into future LDA experiments.

The 3D LDA performed remarkably well for a first test, considering the complexity of the highly three-dimensional flow field associated with a jet in a crossflow. The 14° coupling angle increased the uncertainties in the computation of the lateral velocity component. An analysis of the expected systematic uncertainty pointed out the need for accurate methods of LDA system calibration. An analysis of statistical uncertainty has indicated that errors can be reduced by optimizing the LDA optical system and its associated electronics, thus obtaining higher signal/noise ratios over the frequency range appropriate to the experiment (2-50 MHz for the jet in crossflow). Generally, it is beneficial to increase the number of velocity samples and to minimize the standard deviation of the sampling distribution to more accurately represent the mean lateral velocity. A thorough understanding of the factors that determine the accuracy and limitations of LDA measurements using nonorthogonal channels will significantly improve the quality of data obtained in future LDA applications.

APPENDIX A

DERIVATION OF EQUATION (13)

Equation (13), $\eta = (1 + \cos^2 \phi)^{1/2} / \sin^2 \phi$, is derived as follows. Three assumptions are made:

1. N points of data of measured velocity components V_{VT} and V_{GN} . Measurements are random, nonsimultaneous, and independent

2. Mean estimators are \bar{V}_{VT} and \bar{V}_{GN} and are sample averages over N:

$$\bar{V} = \frac{1}{N} \sum_{i=1}^N V_i$$

3. Standard deviation estimators (ref. 14) are s_{VT} and s_{GN} and

$$s^2 = \frac{1}{N-1} \sum_{i=1}^N (V_i - \bar{V})^2$$

Also,

$$\bar{V} = \frac{\bar{V}_{VT}}{\sin \phi} - \frac{\bar{V}_{GN}}{\tan \phi} \quad (A1)$$

and

$$V_i = \frac{V_{VTi}}{\sin \phi} - \frac{V_{GNi}}{\tan \phi} \quad (A2)$$

Then,

$$\begin{aligned} \delta V_i &= \left(\frac{\partial V_i}{\partial V_{VTi}} \right) \delta V_{VTi} + \left(\frac{\partial V_i}{\partial V_{GNi}} \right) \delta V_{GNi} \\ \delta V_i &= \left(\frac{1}{\sin \phi} \right) \delta V_{VTi} + \left(\frac{1}{\tan \phi} \right) \delta V_{GNi} \end{aligned} \quad (A3)$$

To find s_V :

$$(\delta V_i)^2 = \frac{(\delta V_{VTi})^2}{\sin^2 \phi} + \frac{(\delta V_{GNi})^2}{\tan^2 \phi} + \frac{\delta V_{VTi} \delta V_{GNi}}{\sin \phi \tan \phi} \quad (A4)$$

$$\begin{aligned} \frac{1}{N-1} \sum_{i=1}^N (\delta V_i)^2 &= \frac{\frac{1}{N-1} \sum_{i=1}^N (\delta V_{VTi})^2}{\sin^2 \phi} + \frac{\frac{1}{N-1} \sum_{i=1}^N (\delta V_{GNI})^2}{\tan^2 \phi} \\ &+ \frac{\frac{1}{N-1} \sum_{i=1}^N \delta V_{VTi} \delta V_{GNI}}{\sin \phi \tan \phi} \end{aligned} \quad (A5)$$

Since V_{VTi} and V_{GNI} are independent random measurements,

$$\sum_{i=1}^N \delta V_{VTi} \delta V_{GNI} = 0$$

for enough samples ($N > 30$).

By definition,

$$s_V = \frac{1}{N-1} \sum_{i=1}^N (\delta V_i)^2 \quad (A6)$$

$$s_{VT}^2 = \frac{1}{N-1} \sum_{i=1}^N (\delta V_{VTi})^2 \quad (A7)$$

$$s_{GN}^2 = \frac{1}{N-1} \sum_{i=1}^N (\delta V_{GNI})^2 \quad (A8)$$

Substituting equations (A6)-(A8) into (A5) yields

$$s_V^2 = \frac{s_{VT}^2}{\sin^2 \phi} + \frac{s_{GN}^2}{\tan^2 \phi}$$

The s_{VT} and s_{GN} terms are statistics related to the distribution of measured velocities in the violet and green directions. For smaller coupling angles ($\phi < 30^\circ$), s_{VT} and s_{GN} tend to be of the same magnitude because the measuring directions are nearly the same.

Assuming that $s = s_{VT} \approx s_{GN}$:

$$s_v^2 = \frac{s^2}{\sin^2 \phi} + \frac{s^2}{\tan^2 \phi}$$

$$\frac{s_v}{s} = \left(\frac{1 + \cos^2 \phi}{\sin^2 \phi} \right)^{1/2}$$

$$\eta \equiv \left(\frac{1 + \cos^2 \phi}{\sin^2 \phi} \right)^{1/2} \quad (A9)$$

The distribution of computed velocities \bar{V} is described by the statistics \bar{V} and s_v . The standard deviation s_v is shown to be a factor η higher than the standard deviation s_{GN} or s_{VT} .

Since the value \bar{V} is of primary interest, it is possible to use the statistic s_v to estimate the bounds of uncertainty.

Figure 18 illustrates equation (A9).

APPENDIX B

DERIVATION OF EQUATION (19)

Equation (19), $\Delta\theta(\text{rad}) = z_c/N^{1/2}(s/V_R)\cos\theta[\eta^2 + \tan^2\theta + 2(\tan\theta)/\tan]^{1/2}$ is derived as follows.

In the following derivation, reference is made to figure 6 and the same assumptions defined in appendix A apply. Measured velocities V_{VT} and V_{GN} can be written in terms of the resultant vector magnitude V_R and the angle θ as

$$\left. \begin{aligned} V_{VT} &= V_R \cos(\theta - \phi) \\ V_{GN} &= V_R \cos \theta \end{aligned} \right\} \quad (B1)$$

Equations (B1) can be combined to eliminate V_R , to give

$$\tan \theta = \frac{V_{VT}}{V_{GN}} \left(\frac{1}{\sin \phi} \right) - \left(\frac{1}{\tan \phi} \right) \quad (B2)$$

Assuming that V_{VT} and V_{GN} are independent random variables (refs. 13, 14) then,

$$s_\theta^2 = \left(\frac{\partial \theta}{\partial V_{VT}} \right)^2 s_{VT}^2 + \left(\frac{\partial \theta}{\partial V_{GN}} \right)^2 s_{GN}^2 \quad (B3)$$

From equation (B2):

$$\begin{aligned} \frac{\partial \theta}{\partial V_{VT}} &= \frac{\cos^2 \theta}{V_{GN} \sin \phi} \\ \frac{\partial \theta}{\partial V_{GN}} &= -\frac{V_{VT} \cos^2 \theta}{V_{GN}^2 \sin \phi} \end{aligned}$$

Substituting into equation (B3) yields

$$s_\theta^2 = \frac{\cos^4 \theta}{V_{GN}^2 \sin^2 \phi} \left[s_{VT}^2 + \left(\frac{V_{VT}}{V_{GN}} \right)^2 s_{GN}^2 \right]$$

From equations (B1),

$$V_R = \frac{V_{GN}}{\cos \theta} \quad \text{and} \quad \frac{V_{VT}}{V_{GN}} = \frac{\cos(\theta - \phi)}{\cos \theta}$$

so that

$$s_{\theta}^2 = \frac{\cos^2 \theta}{V_R^2 \sin^2 \phi} \left[s_{VT}^2 + \frac{\cos^2(\theta - \phi)}{\cos^2 \theta} s_{GN}^2 \right]$$

Using the assumption that $s = s_{VT} = s_{GN}$ (as in appendix A), then

$$s_{\theta}^2 = \frac{s^2 \cos^2 \theta}{V_R^2} \left(\frac{1 + \cos^2 \phi}{\sin^2 \phi} + \tan^2 \theta + \frac{2 \tan \theta}{\tan \phi} \right)$$

The first term inside the brackets is exactly η^2 , which was derived in appendix A; hence

$$s_{\theta} = \frac{s \cos \theta}{V_R} \left(\eta^2 + \tan^2 \theta + \frac{2 \tan \theta}{\tan \phi} \right)^{1/2} \quad (B4)$$

For N samples, the estimated error $\Delta \theta$ in the angle θ with a 95% confidence level is

$$\Delta \theta (\text{rad}) = \frac{z_c s_{\theta}}{N^{1/2}} = \frac{z_c}{N^{1/2}} \frac{s}{V_R} \cos \theta \left(\eta^2 + \tan^2 \theta + \frac{2 \tan \theta}{\tan \phi} \right)^{1/2} \quad (B5)$$

Figures 4 and 5 graphically illustrate equation (B5).

REFERENCES

1. Rudd, M. J.: A New Theoretical Model for the Laser Dopplermeter. J. Sci. Instrum. (J. Phys. E), Series 2, vol. 2, 1969, pp. 55-58.
2. Von Stein, H. D.; and Pfeifer, H. J.: A Doppler Difference Method for Velocity Measurement. Int. J. Sci. Metrology, vol. 5, no. 2, 1969, pp. 59-61.
3. Mayo, W. J., Jr.: Simplified Laser Doppler Velocimeter. J. Phys. E, vol. 3, 1970, pp. 235-237.
4. Grant, G. R.; and Orloff, K. L.: Two Color Dual-Beam Backscatter Laser Doppler Velocimeter. Appl. Opt., vol. 12, no. 12, 1973, pp. 2913-2916.
5. Fridman, J. D.; Huffaker, R. M.; and Kinnard, R. J.: Laser Doppler System Measures Three-Dimensional Vector Velocity and Turbulence. Laser Focus, vol. 4, no. 21, 1968, p. 34.
6. Orloff, K. L.; and Logan, S. E.: Confocal Backscatter Laser Velocimeter with On-Axis Sensitivity. Appl. Opt., vol. 12, no. 10, 1973, pp. 2477-2481.
7. Siegman, A. E.: The Antenna Properties of Optical Heterodyne Receivers. Appl. Opt., vol. 5, no. 10, 1966, pp. 1583-1594.
8. Abbiss, J. B.; Sharpe, P. R.; and Wright, M. P.: Experiments Using a Three-Component Laser-Anemometry System on a Subsonic Flow with Vorticity. Royal Aircraft Establishment, Technical Report 80081, June 1980.
9. Yanta, W. J.: A Three-Dimensional Laser Doppler Velocimeter for Use in Wind Tunnels. Proceedings of the 8th International Congress of Instrumentation in Aerospace Simulation Facilities, Monterey, Calif., Sept. 1979.
10. Orloff, K. L.; and Olson, L. E.: High-Resolution LDA Measurements of Reynolds Stress in Boundary Layers and Wakes. AIAA Paper No. 80-0436, AIAA 11th Aerodynamic Testing Conference, March 18-20, 1980, Colorado Springs, Colo.
11. Corsiglia, V. R.; Iverson, J. D.; and Orloff, K. L.: Laser Velocimeter Surveys of Merging Vortices in a Wind Tunnel. J. Aircraft, vol. 15, no. 11, Nov. 1978, pp. 762-768.
12. Yanta, W. J.; and Smith, R. A.: Measurements of Turbulence-Transport Properties with a Laser Doppler Velocimeter. AIAA Paper No. 73-169, AIAA 11th Aerospace Sciences Meeting, Jan. 10-12, 1973, Washington, D.C.

13. Baird, D. C.: Experimentation. Prentice-Hall, New Jersey, 1962.

14. Speigel, M. R.: Probability and Statistics. McGraw-Hill, New York, 1975.

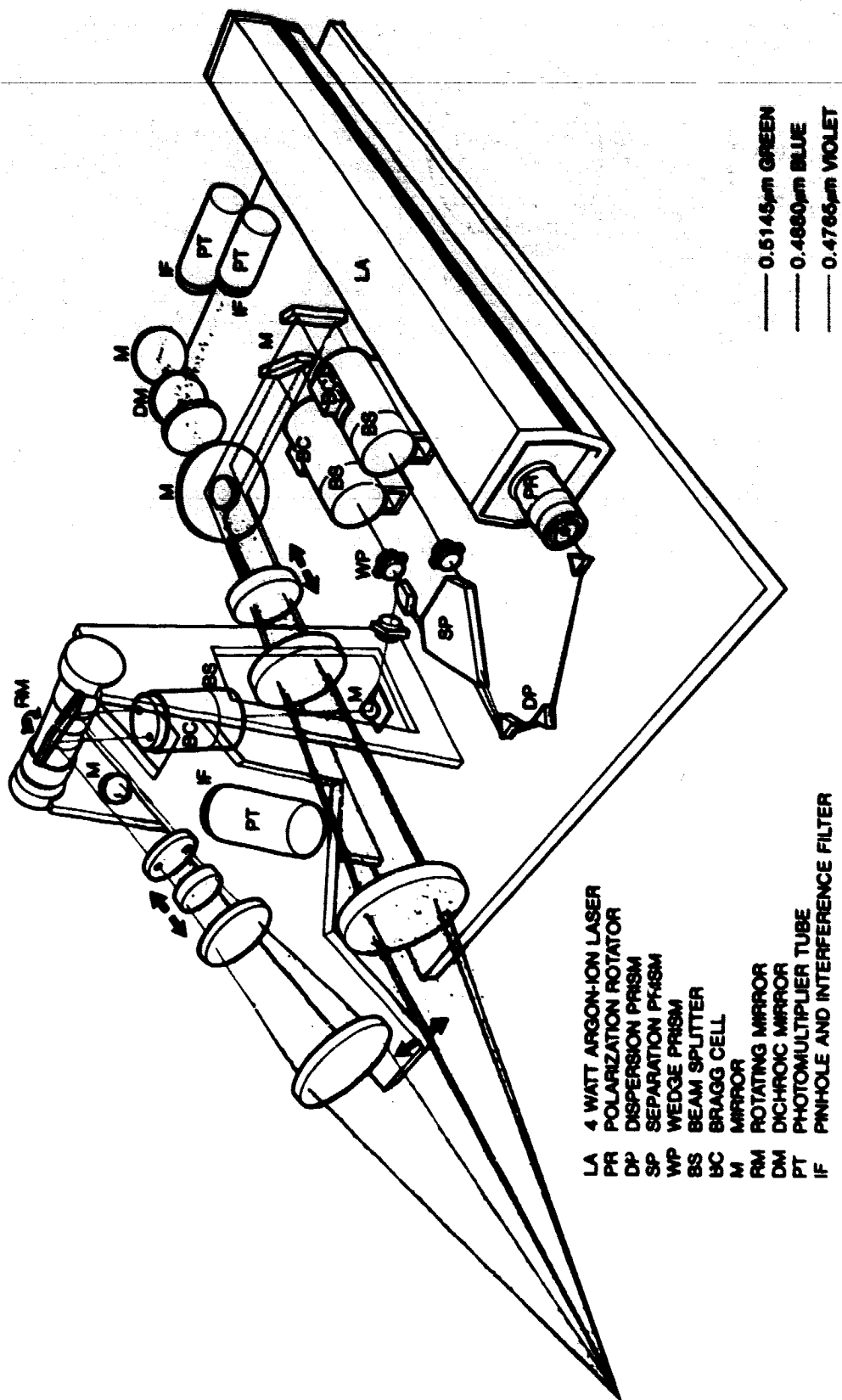


Figure 1.- 3D laser Doppler anemometer.

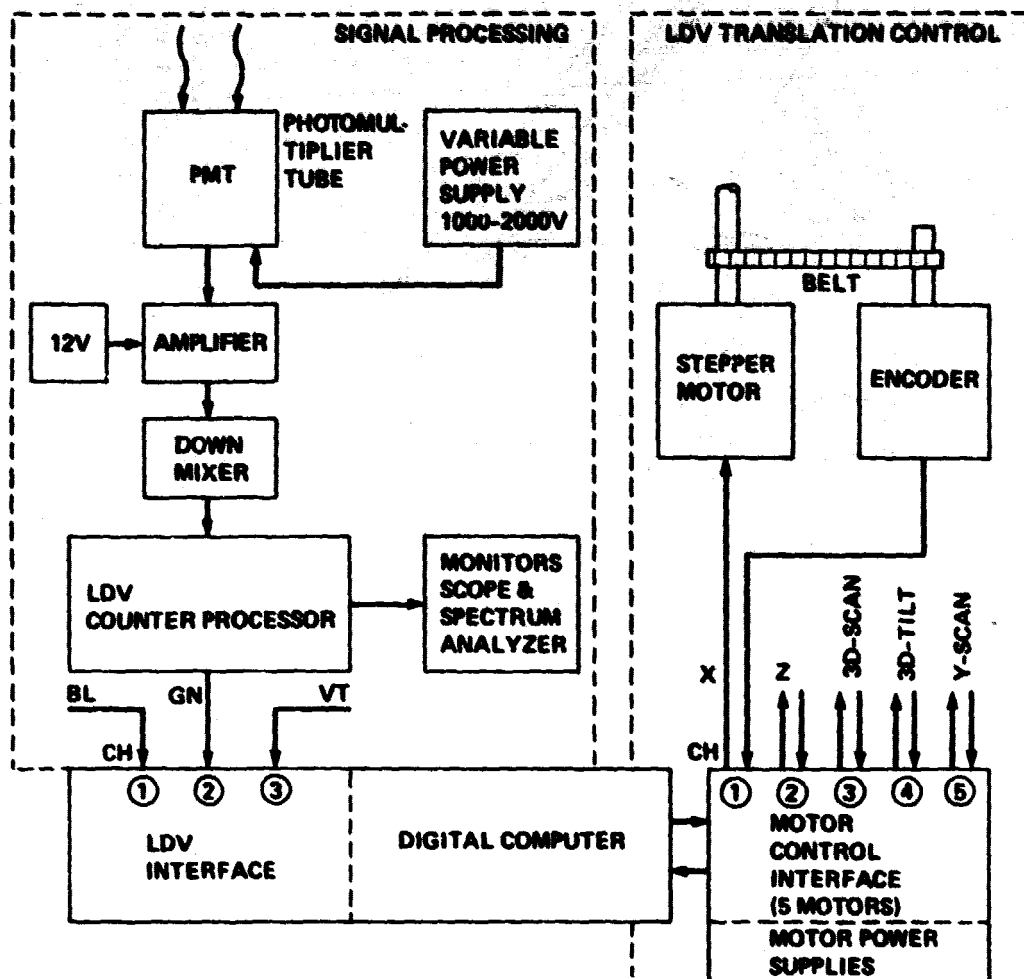


Figure 2.- System electronics.

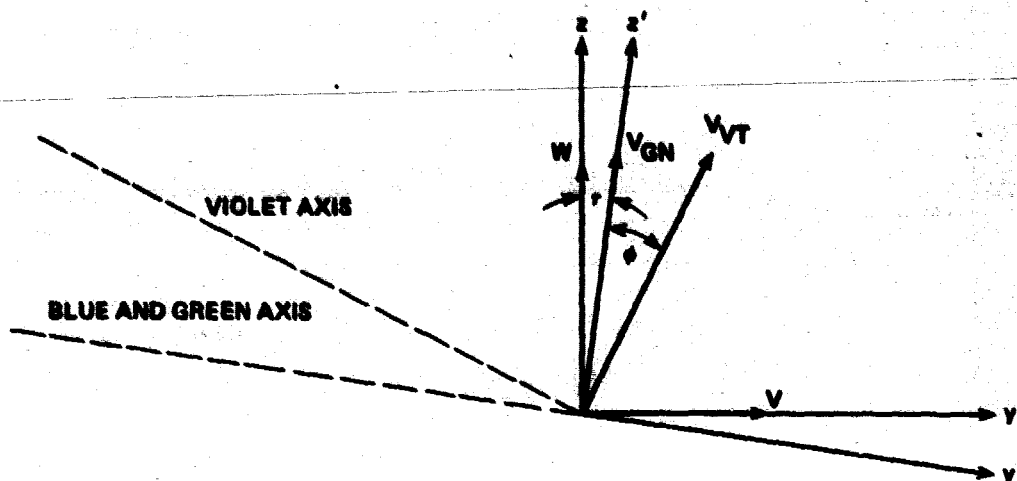


Figure 3.- Resolving vertical and lateral velocities V and W from measured velocities V_{GN} and V_{VT} .

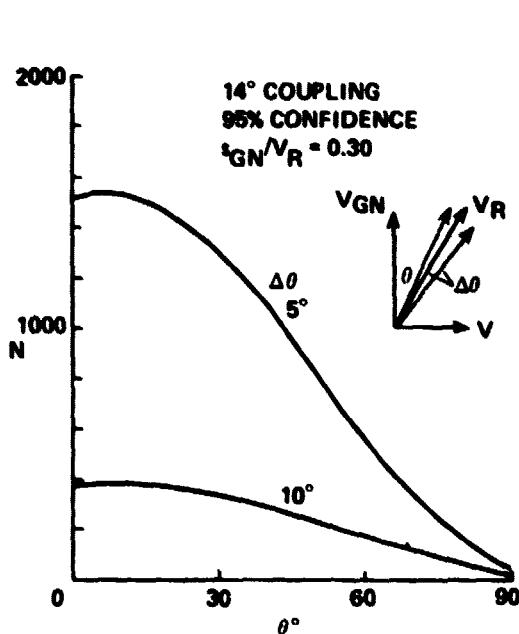


Figure 4.- Number of samples N required to resolve the in-plane vector V_R at various angles θ to within $\pm\Delta\theta^\circ$.

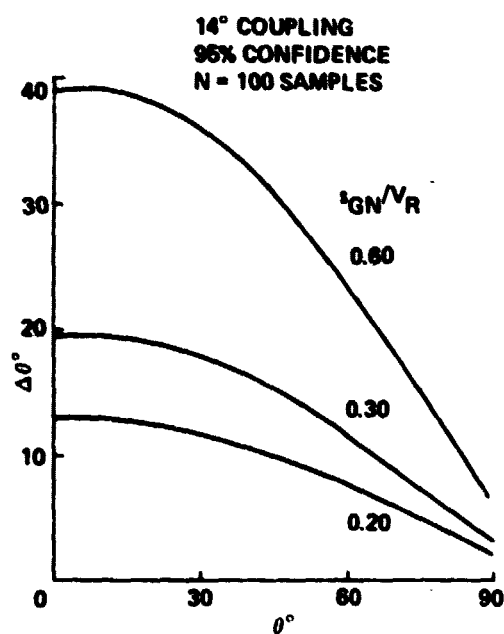


Figure 5.- Directional uncertainty $\Delta\theta$ as a function of in-plane vector angle θ for various relative standard deviations.

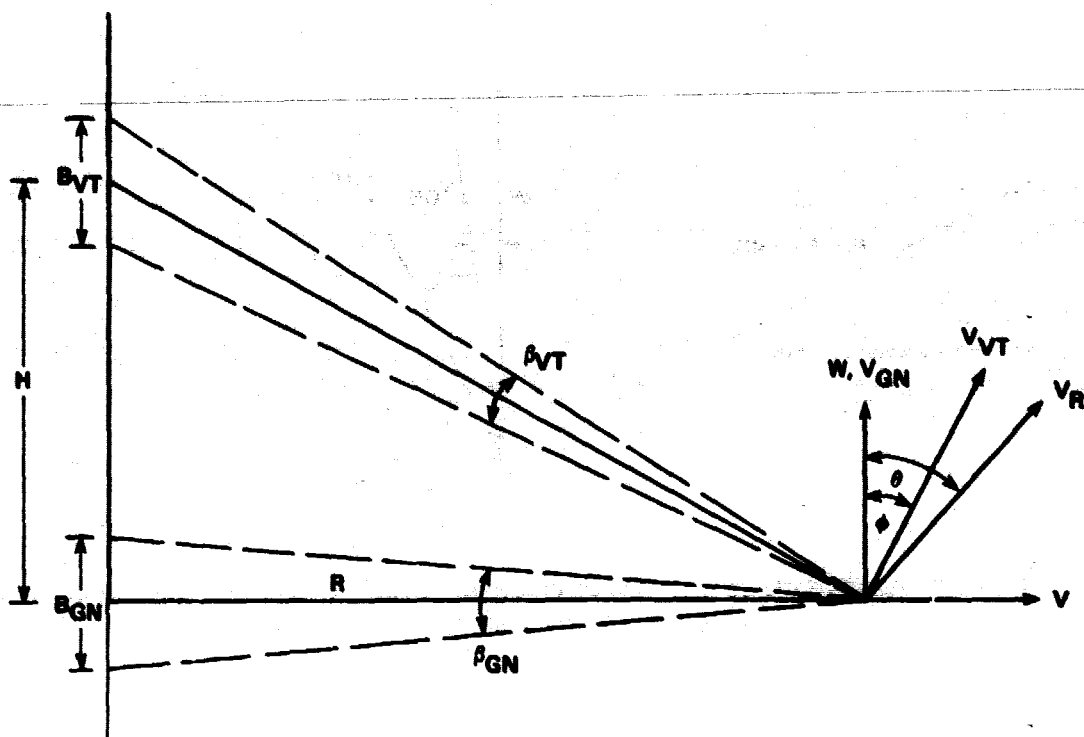


Figure 6.- Calibration parameters for the 3D LDA systematic uncertainty analysis.

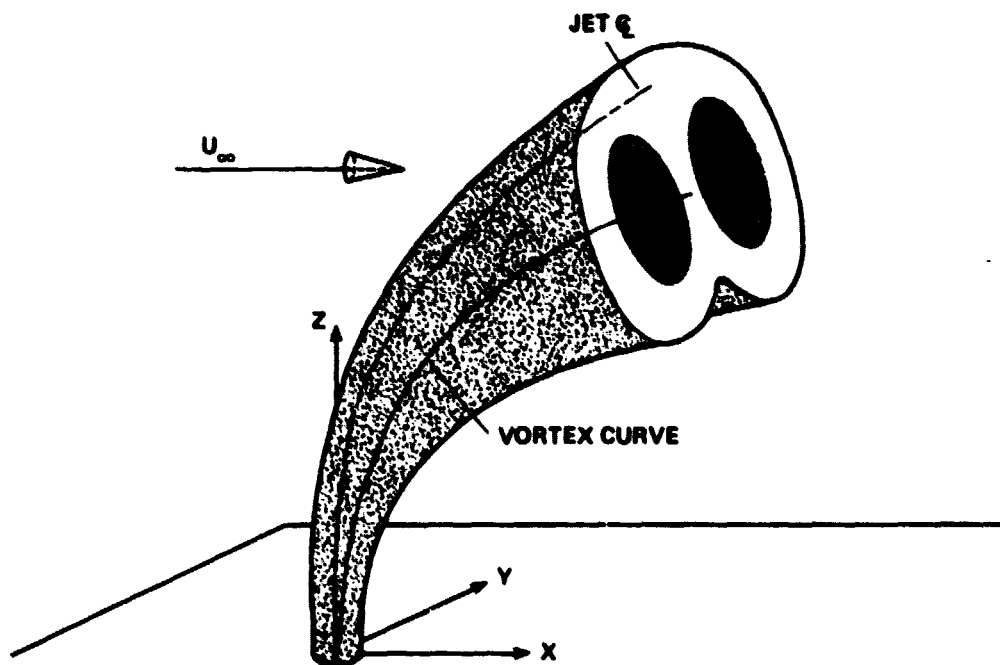


Figure 7.- Sketch of a jet in a crossflow.

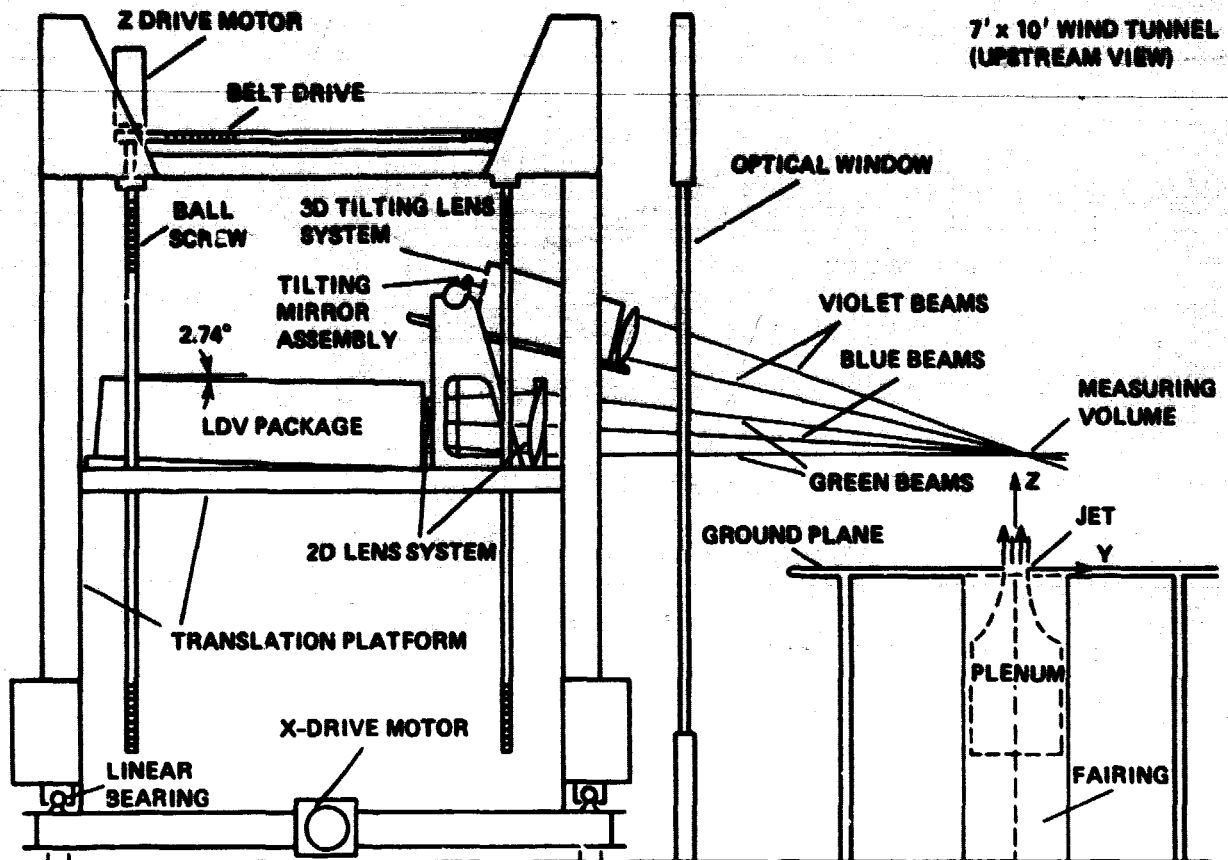


Figure 8.- 3D LDA translation platform and tunnel installation for the jet-in-a-crossflow test.

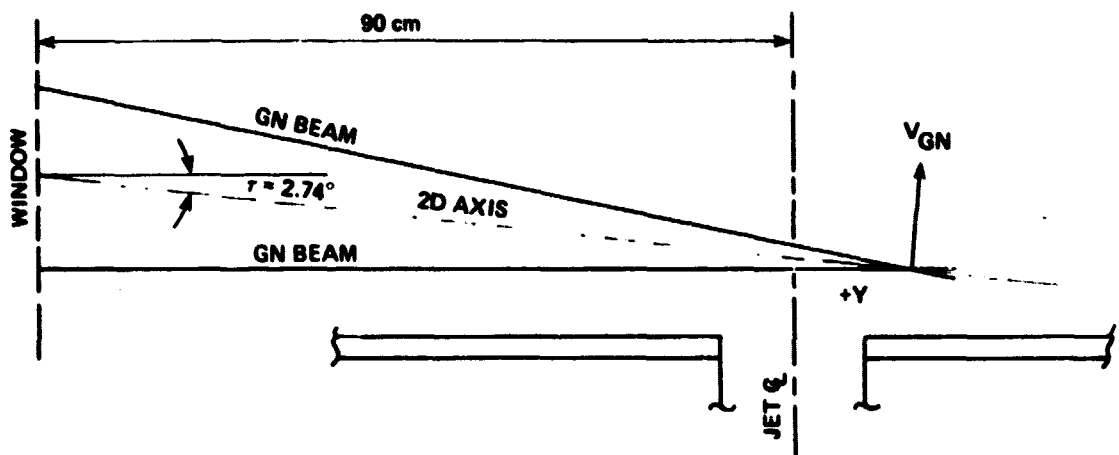


Figure 9.- Inclined 2D scanning axis.

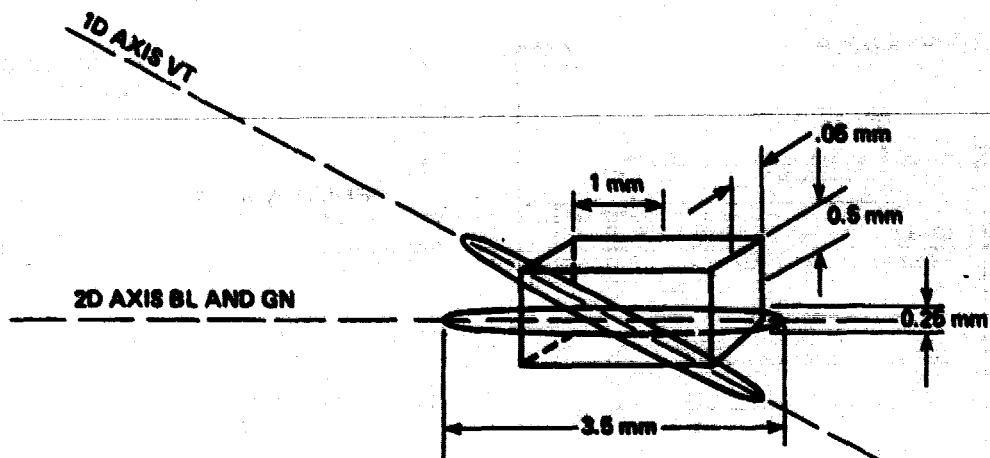


Figure 10.- Measuring volume size and positioning uncertainty.

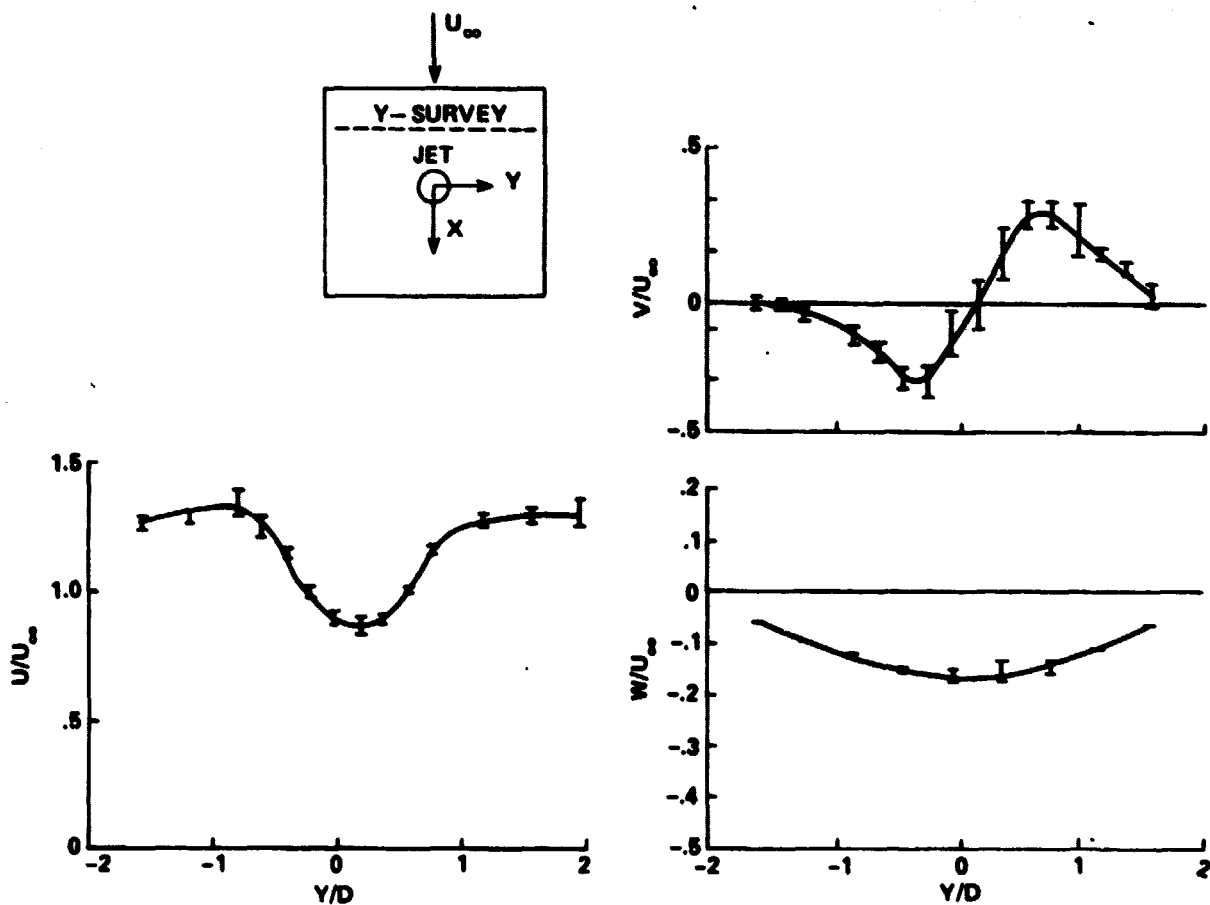


Figure 11.- 3D mean velocities upstream of the jet in a crossflow.

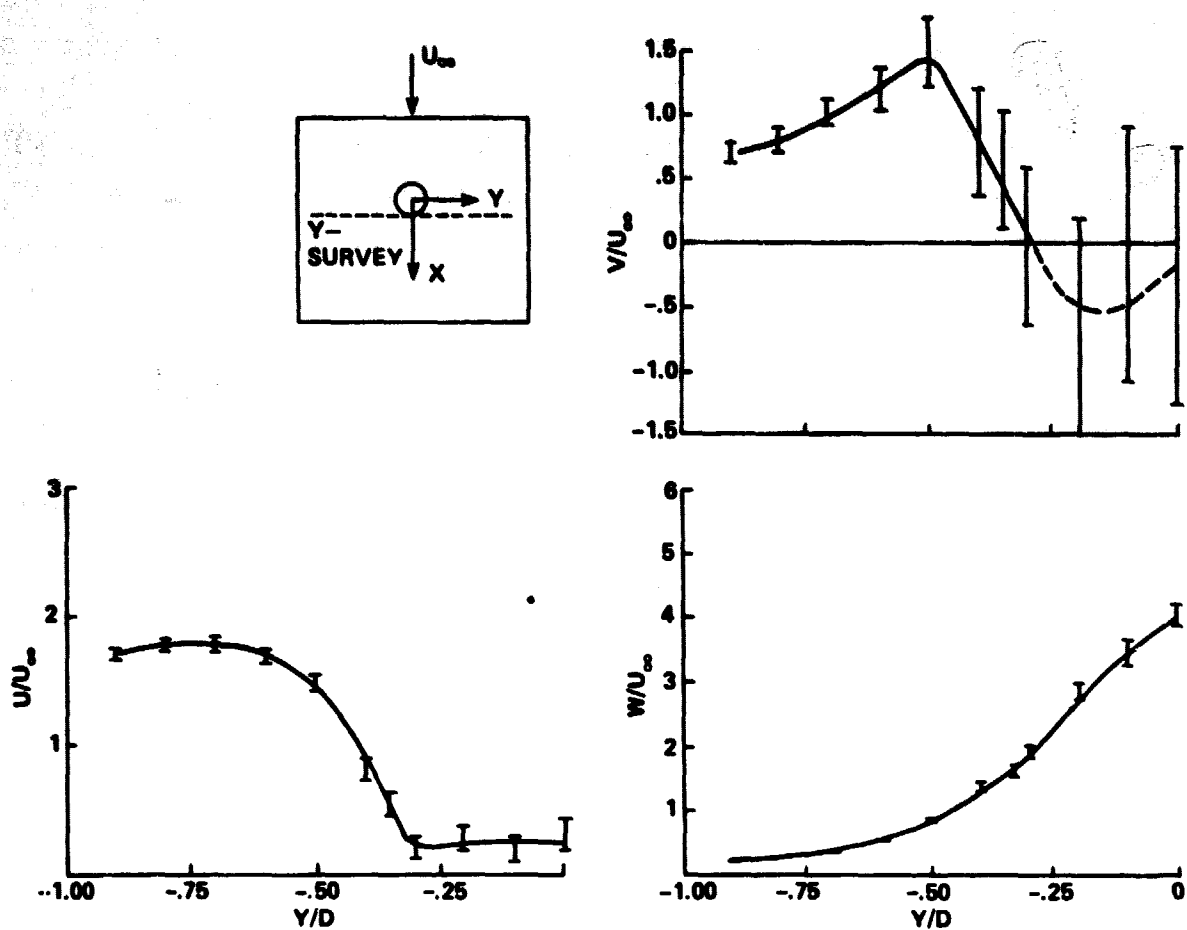


Figure 12.- 3D mean velocities through aft section of a jet in a crossflow.

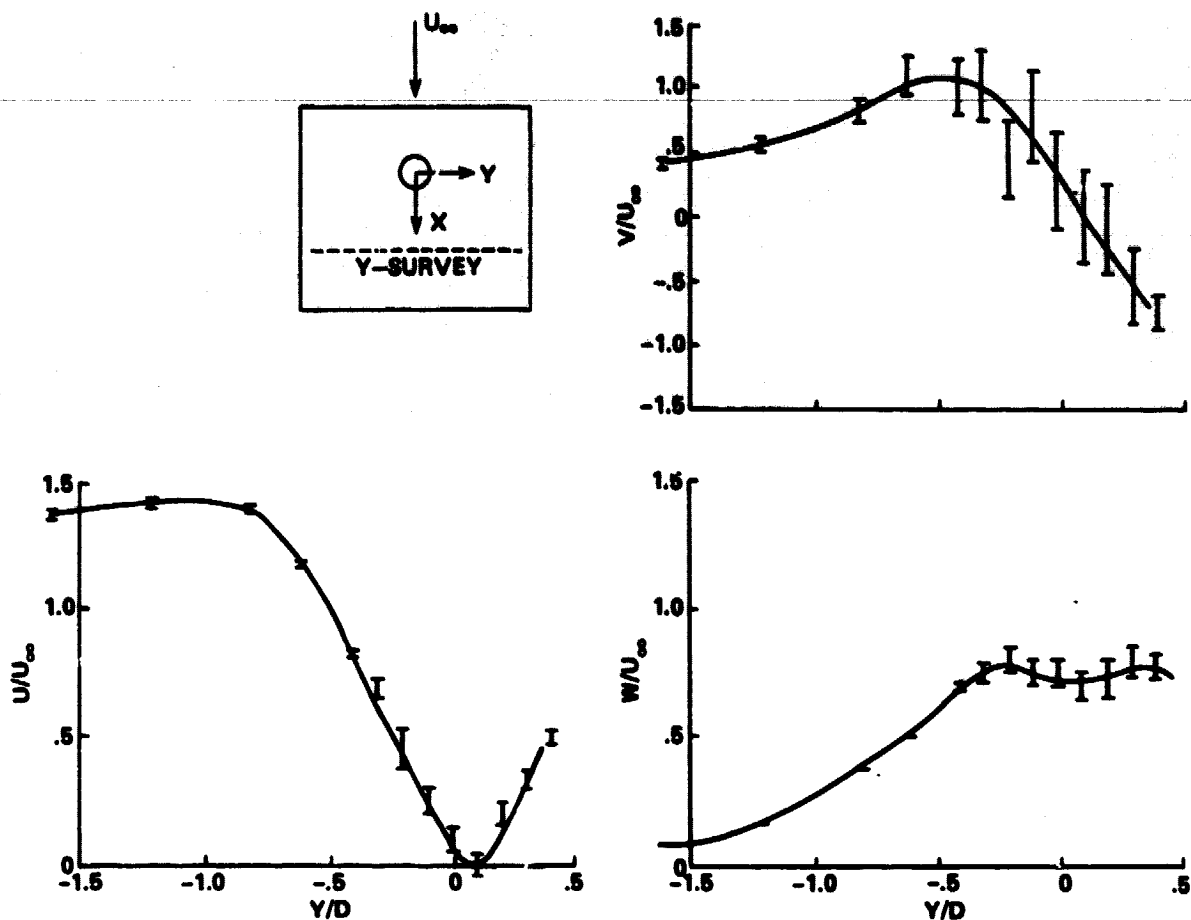


Figure 13.- 3D mean velocities in the wake region of the jet in a crossflow.

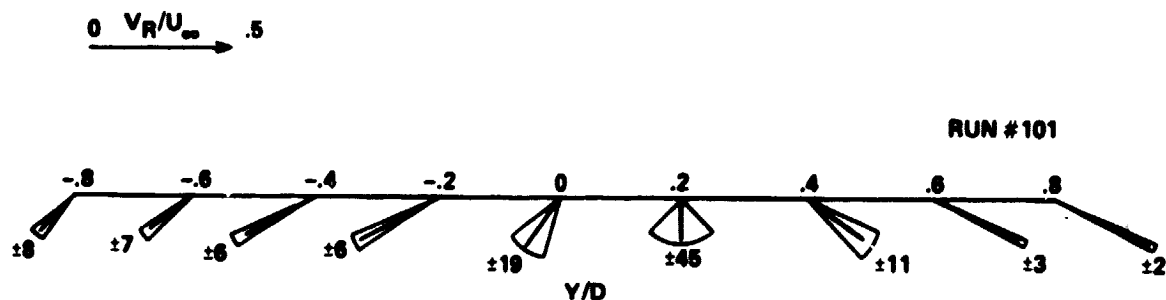


Figure 14.- Statistical directional uncertainties of the velocity vectors V_R in the y - z plane: 95% confidence level; derived from data in Fig. 11.

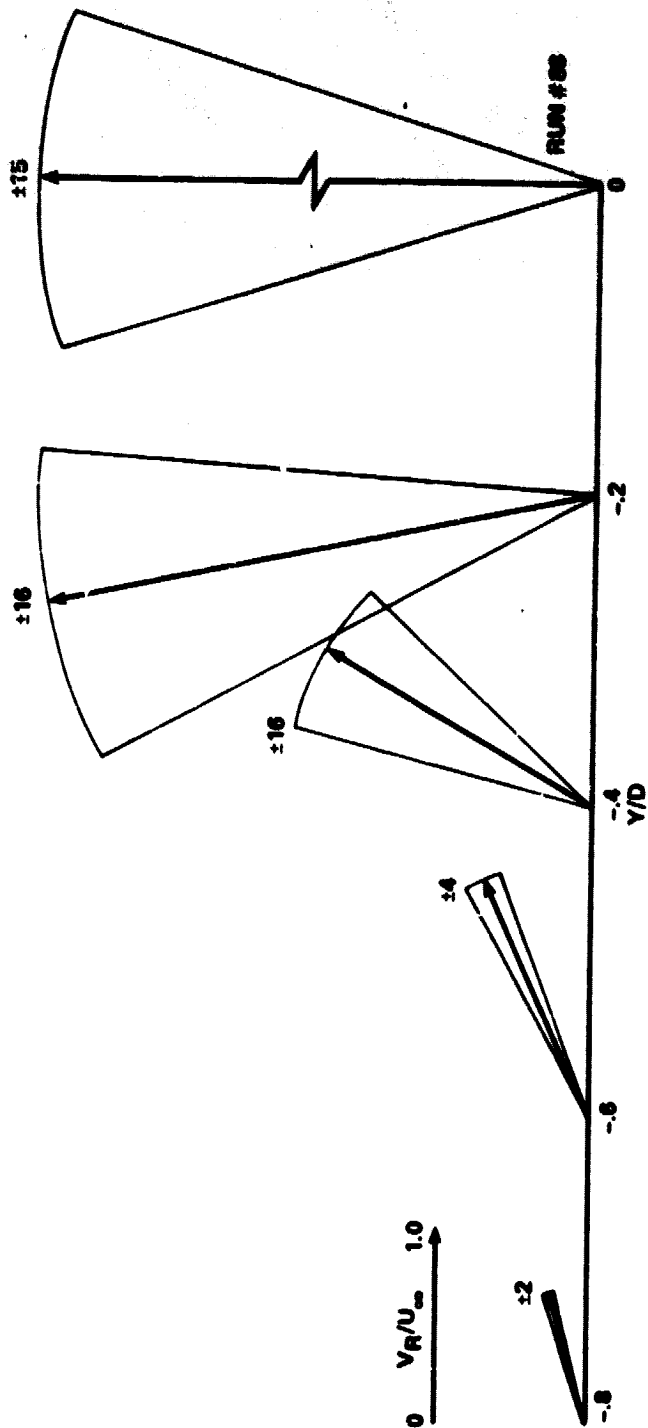


Figure 15.- Statistical directional uncertainties of the velocity vectors V_R in the y - z plane: 95% confidence level; derived from data in Fig. 12.

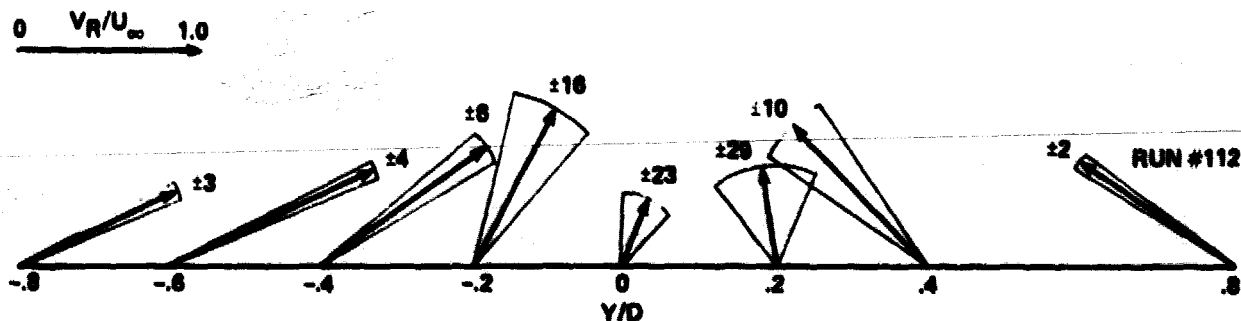


Figure 16.- Statistical directional uncertainties of the velocity vectors V_R in the y - z plane: 95% confidence level; derived from data in fig. 13.

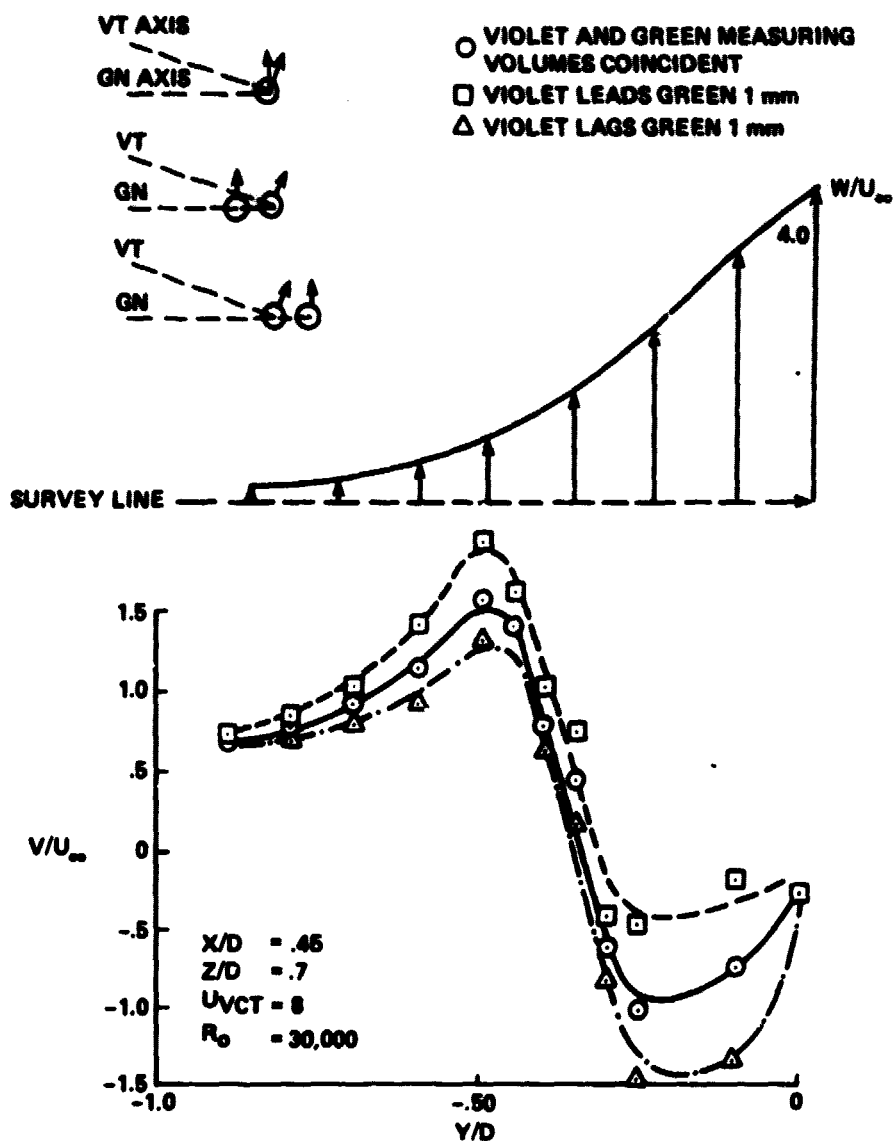


Figure 17.- Simulated differences in lateral flow due to misalignment of green and violet beams.

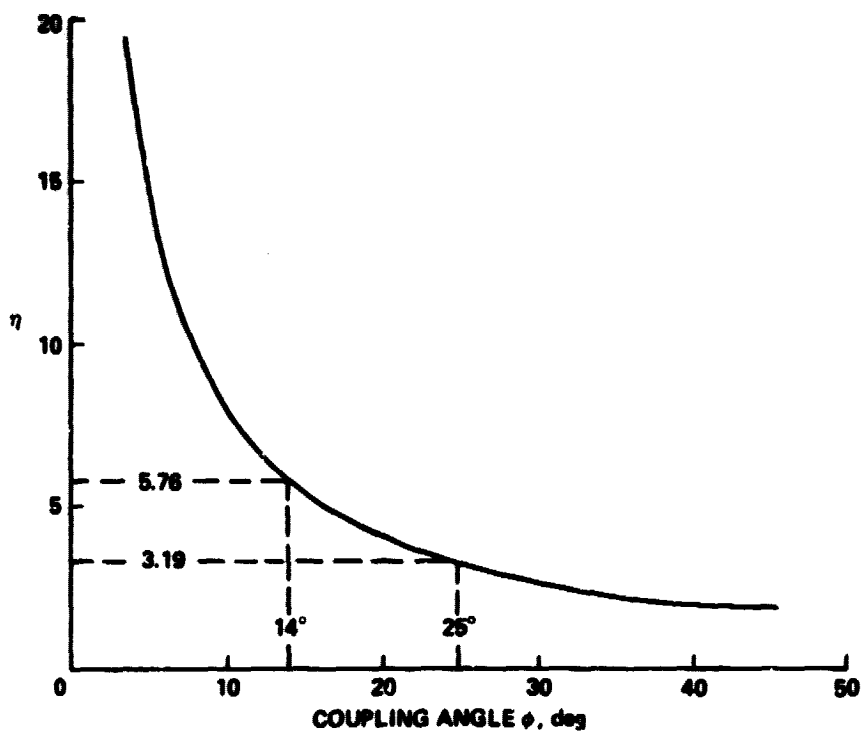


Figure 18.- Ratio η representing the standard deviation of the computed lateral velocity distribution with respect to the standard deviation of two independently measured velocity distributions coupled by an angle ϕ .